JACS
JOURNAL OF THE AMERICAN CHEMICAL SOCIETY
Article
pubs.acs.org/JACS

The Reaction Mechanism with Free Energy Barriers at Constant Potentials for the Oxygen Evolution Reaction at the IrO_2 (110) Surface

Yuan Ping,[*,†,‡,§] Robert J. Nielsen,[†,‡] and William A. Goddard III[*,†,‡]

[†]Joint Center for Artificial Photosynthesis and [‡]Materials and Process SimulationCenter, California Institute of Technology, Pasadena, California 91125, United States

Supporting Information

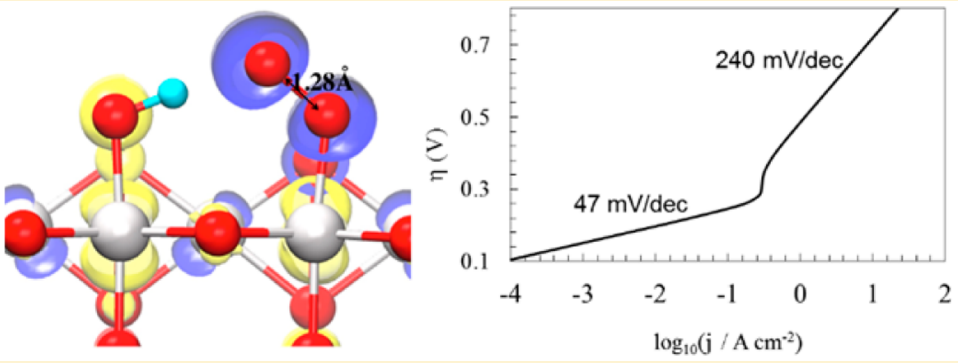

ABSTRACT: How to efficiently oxidize H_2O to O_2 (oxygen evolution reaction, OER) in photoelectrochemical cells (PEC) is a great challenge due to its complex charge transfer process, high overpotential, and corrosion. So far no OER mechanism has been fully explained atomistically with both thermodynamic and kinetics. IrO_2 is the only known OER catalyst with both high catalytic activity and stability in acidic conditions. This is important because PEC experiments often operate at extreme pH conditions. In this work, we performed first-principles calculations integrated with implicit solvation at constant potentials to examine the detailed atomistic reaction mechanism of OER at the IrO_2 (110) surface. We determined the surface phase diagram, explored the possible reaction pathways including kinetic barriers, and computed reaction rates based on the microkinetic models. This allowed us to resolve several long-standing puzzles about the atomistic OER mechanism.

1. INTRODUCTION

Artificial photosynthesis is one of the most promising strategies to convert sunlight to clean fuels.[1] The oxygen evolution reaction (OER) through water oxidation is the most critical step for both water splitting[2,3] and CO_2 reduction.[4] Understanding the atomistic details of the OER mechanism for heterogonous catalysts is extremely important for both interpreting electrochemical measurements and designing new catalysts. Most of the previous theoretical studies of OER catalysts mainly focused on the thermodynamic properties of the reaction intermediates without considering their free energy barriers (including transition states) and kinetic reaction rates in details.[5−7] Indeed most quantum mechanics (QM) calculations have been performed with constant total number of electrons (constant charge), instead of the constant potential conditions of the experiments. The difficulty of QM for treating charged systems in solution has made such constant potential calculations a formidable task until the recent implementation of the constant potential DFT in conjunction with the CANDLE implicit solvent method by Sundararamen et al.[8] and applied recently to CO_2 reduction at Cu surfaces.[9]

IrO_2 is the only active OER catalyst that is relatively stable in the acidic condition, which is critical for integration with photoanodes and optimal PEC efficiency.[10] Recently, we found that the morphology of IrO_2 can modify the catalyst-photoanode interfacial energetics dramatically when in contact with water.[11] However, the mechanistic details of IrO_2 including kinetic barriers at the constant potential condition have not been reported. Here with IrO_2 our prototype, we report the first study of atomistic mechanism for a heterogeneous OER catalyst including free energy barriers at constant potential conditions. We address here: (1) What is the rate-determining step (RDS) of the IrO_2 OER reaction? (2) How does the constant potential condition affect the reaction barriers compared with the standard constant charge conditions? (3) How does the QM overpotential compare with experiments at a particular electrical current? (4) What does the mechanism suggest for improving OER catalytic efficiency?

Received: July 21, 2016
Published: December 9, 2016

DOI: 10.1021/jacs.6b07557
J. Am. Chem. Soc. 2017, 139, 149−155

The following sections are organized as follows: Computational Methods, Results and Discussion, and Conclusions and Outlook at the end.

2. COMPUTATIONAL METHODS

We performed first-principles calculations of IrO_2 (110) surface with plane wave basis sets and GBRV ultrasoft pseudopotentials[12] within the Quantum-Espresso package.[13] We chose IrO_2 (110) surface because it has been shown theoretically to be the most stable surface[11] similar to other rutile structures, TiO_2 and RuO_2. We constructed five layer slab with inversion-symmetry to avoid net dipoles in the cell (the atomic structure of the IrO_2 (110) slab can be found in Figure S1), and we used 12 Å vacuum to avoid periodic image interactions. We used spin-polarized PBE exchange correlation functional along with the DFT-D2 pair potential dispersion corrections.[14] See the Supporting Information (SI) for further computational details for the density functional theory (DFT) calculations.

We used the Climbing Image-Nudged Elastic Band[15] (CI-NEB) method to locate the transition state, as implemented in Quantum Espresso. The phonon vibrational frequencies for Gibbs free energy calculations are obtained by Density Functional Perturbation Theory (DFPT).[16] The vibrational contributions to free energies have been included for both surfaces and molecules. To compute free energy change of elementary reaction steps involving gaseous or liquid molecules, such as water and hydrogen, we took into account the contributions of rotation, translation, and vibration to the free molecule, which we obtained from Jaguar package[17] as well as the solvation energy of water molecule in liquid water (2.05 kcal/mol). The free energy of gas phase O_2 is derived as $G[O_2] = 4.92(eV) + 2G[H_2O] - 2G[H_2]$ by utilizing experimental Gibbs free energy of the reaction $(2H_2O(l) \rightarrow O_2(g)+2H_2(g))$ at the standard conditions.[18] See the SI for further details of DFPT and Jaguar calculations.

We used the new CANDLE implicit solvation model, which has been shown to perform successfully for various metallic and ionic surfaces.[19,20] We computed the grand free energy at the constant electrochemical potential along with the implicit solvation model, in which the charged surfaces can be effectively screened by the ionic response in solution as implemented in JDFTx.[8,21,22] Computational details of JDFTx can be found in SI.

3. RESULTS AND DISCUSSION

3.1. Surface Diagram of IrO_2 (110). Before studying the reaction mechanism, it is essential to understand the equilibrium surface structure under OER operating conditions. The IrO_2 surface is unstable at basic conditions (the OER efficiency decays significantly after 1 h), but recent studies[24,25] show that it remains stable at pH = 0 over several hours. Therefore, we focus on the surface diagram of IrO_2 at pH = 0 condition.

For the stoichiometric IrO_2 (110) surface, half of the surface Ir atoms are 5 coordinated. We showed that H_2O binds strongly (by ~1.7 eV/H_2O in liquid water) at this surface[20] and the H_2O molecules spontaneously dissociate to form − OH at the unsaturated Ir (Ir-5c) and − OH at the bridging O (as shown in Figure 1 "OH" surface structure), independent of the starting surface water configurations (see SI Figure S2). With increasing the applied potentials, the OH terminated surface is oxidized to gradually lose H atoms. We computed the surface free energy as following:

$$\Delta G_{surf} = G_{surf-sol} - G_{bulk} - NG_{H_2O-sol} + nG_{H+}(pH) + nG_e(U) = G_{surf-sol} - G_{bulk} - NG_{H_2O-sol} + \frac{n}{2}G_{H_2}(1\ atm, 298\ K) + ne(U - NHE) \quad (1)$$

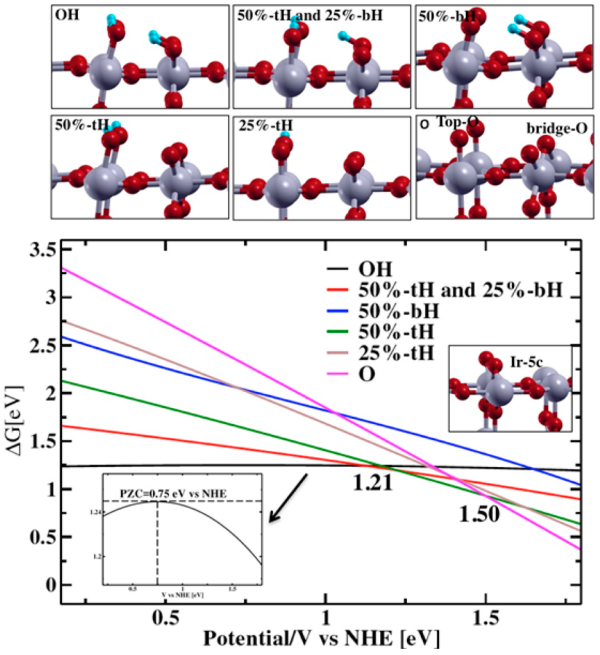

Figure 1. Surface phase diagram of IrO_2 (110) with one monolayer of H_2O as a function of applied potentials. The top six panels show the surface structures with different OH terminations; the bottom panel shows the surface diagram. Black curve, OH terminated surface; red curve, 75% OH terminated surface with 50% top O and 25% bridging O; blue curve, 50% OH terminated surface with bridging O; dark green curve, 50% OH terminated surface with top O; gray curve, 25% OH terminated surface with top O; purple curve, O terminated surface. The inner figure at the bottom left shows the zoom-in of the black curve (OH terminated surface) where the crossing of horizontal tangential line and the vertical line shows the potential of zero charge of IrO_2 (110) surface in solution at pH = 0. The purple and dark green lines cross at 1.50 eV and the red and dark green lines cross at 1.21 eV. The surface structure inside the surface diagram is the stoichiometric (110) IrO_2.

where G is the grand free energy including $N_e\mu_e$ (N_e is the number of electrons at a fixed potential and μ_e is the electron chemical potential); "surf-sol" denotes the solvated (110) IrO_2 surface with one layer of explicit H_2O under applied potentials; "bulk"denotes the pristine bulk IrO_2; "H_2O-sol" denotes solvated water molecule; N is the number of explicit water molecules in the first water layer; n is the number of H atoms removed from the pristine IrO_2 surface plus a layer of water molecules for a particular surface structure. We used the equilibrium relationship at the standard conditions, $^1/_2G_{H_2}$ (1 atm, 298 K) = G_{H+} (pH = 0) + G_e (NHE), in order to set the reference potentials to that of the normal hydrogen electrode (NHE).[23] Since we consider pH = 0, a free energy correction related to pH is not needed. Figure 1 shows that above 1.50 eV (the experimental OER operating potential is around 1.53 eV), the most stable surface is the O terminated surface; however, between 1.21 and 1.50 eV, the 50% OH terminated surface with two H at the top O has the lowest surface energy. If instead we use the constant charge condition (as in most previous studies[5,6,23]), the free energy of the − OH terminated surface (bare IrO_2 surface + one monolayer water) will not depend on the potential (constant at all potentials), because there are no extra electrons exchanging with the reservoir (or n is equal to zero and G denotes Helmholtz free energy under constant charge condition, independent of electron chemical potential

DOI: 10.1021/jacs.6b07557
J. Am. Chem. Soc. 2017, 139, 149−155

explicitly). However, for the constant potential condition (the experimental condition), the −OH terminated surface can be charged depending on the applied potential because the grand free energy G explicitly depends on the electron chemical potential as discussed earlier. The potential at which the surface free energy has zero first order derivative with respect to the electron chemical potential is the potential of zero charge of this surface (PZC); which we calculated to be 0.75 eV vs NHE for the −OH terminated IrO_2 (110) surface in water using PBE +D2).

3.2. Thermodynamics of OER Reaction. *3.2.1. Reaction Path at U > 1.50 eV vs NHE.* As discussed above, at the experimental operating condition U > 1.50 eV vs NHE, we calculate that the most stable surface structure of IrO_2 (110) is the fully O terminated surface (as shown in Figure 1). We will study the reaction mechanism starting from this surface.

From our spin-polarized PBE+D2 calculations, we found that the most stable O terminated surface, has 0.86 unpaired spin on the top O atoms (Lowdin charge; the Ir under the top O has 0.51 unpaired spin; the bridging O has close to zero spin), indicating that the top O atoms have radical character and provide the active sites to form the new O−O bonds that are essential for O_2 production. Next we performed detailed calculations to validate this expectation.

In order to form an O−O bond at the IrO_2 (110) O terminated surface, there are two possible mechanisms: (1) two neighboring O atoms couple and form a new O−O bond and (2) a solvent water molecule attacks the surface O to form an O−O bond.

For mechanism 1, we found that O−O coupling between a top O and a bridging O is unstable (the O−O bond breaks apart during geometry optimization), while it is thermodynamically unfavorable between two neighboring top O atoms (the formation of O−O bond costs 0.62 eV free energy (detailed structure can be found in SI, Figure S6), which costs much more energy compared to the reaction intermediates in mechanism 2 as shown later). Therefore, we focus on the mechanism 2 involving an aqueous water attacking the surface O and dissociating.

We compared the free energy of all possible positions of dissociated H_2O and found both −OOH and −OH bonds prefer to form at the top O atoms (0.21 eV more favorable than −OOH at the top O and −OH at the bridging O; 0.51 eV more favorable than −OOH at the bridging O, −OH at the top O; 0.86 eV more favorable than both −OOH and −OH at the bridging O). This is consistent with the indication of radical characters at the top O atoms at O terminated (110) IrO_2 surface as discussed above, which is more favorable than usual for the site to form a new bond to other atoms.

Figure 2 shows the reaction intermediates and transition state structures as well as their free energy profile computed at the constant potential condition (more details can be found in the SI, Table S1). The difference of free energy barriers and reaction energies between at the constant charge and constant potential conditions varies as a function of applied potential (for details, see the SI, Table S1). Most importantly, at the constant potential condition, the steps that are electrochemically independent at the constant charge condition *become dependent on the electrochemical potential.* For example, the first water dissociation step (shown in Figure 2 reaction 1 → 2) depends strongly on the electrochemical potential (as shown in Figure 3) with a slope of −0.5, which indicates that 0.5 electrons are depleted from the IrO_2 surface in this process.

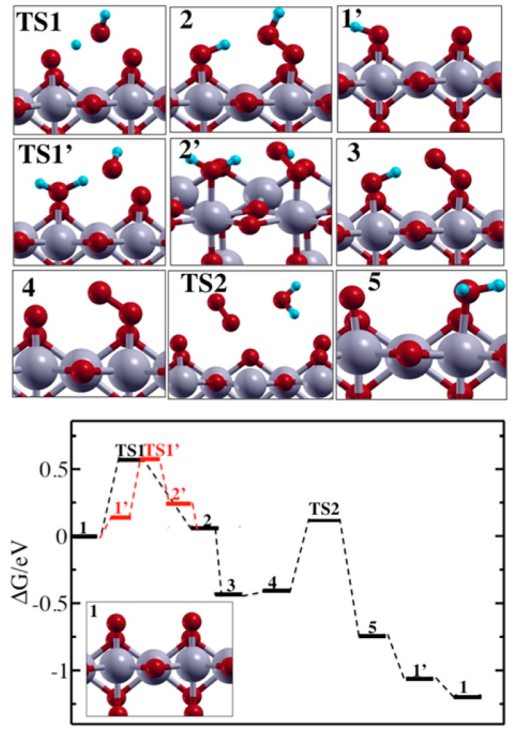

Figure 2. Optimized structure and free energy profile of intermediates and transition states of water dissociation reaction at U = 1.53 eV vs NHE. Red balls are O; blue balls are H; silver balls are Ir.

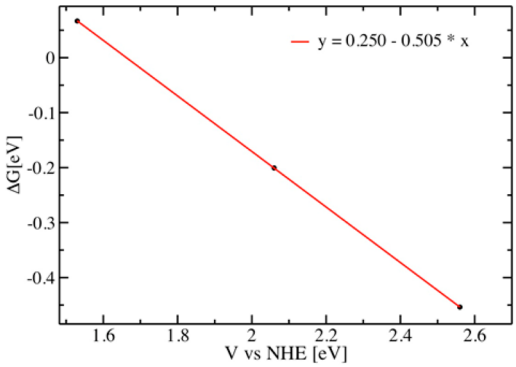

Figure 3. Free energy change of the water dissociation step (reaction 1 → 2 in Figure 2) as a function of the applied potential vs NHE by the constant potential calculations; black dots, calculated; red line, linear regression of black dots.

This is completely neglected in the constant charge calculation—in fact, we found that at the constant charge condition the work function decreases by 1 eV after one water molecule dissociates at the O terminated surface (or the Fermi level of the surface is 1 eV closer to the vacuum; for details, see the SI, Figure S4); therefore, the catalyst IrO_2 surface needs to lose electrons to the electrode in order to keep the Fermi level constant before and after the water dissociation at the surface. Moreover, the large variation of work function during the water dissociation reaction process at the constant charge condition indicates the possible large discrepancy from the experimental constant potential condition. In addition, we note that the free energy of the transition states (between two fixed intermediates) also follow the linear dependence with applied potentials (for details, see the SI, Figure S5).

DOI: 10.1021/jacs.6b07557
J. Am. Chem. Soc. 2017, 139, 149−155

For an external potential of U = 1.53 eV, we found that all reaction steps are exothermic (the black reaction path), showing that OER is favorable at this potential (consistent with the experimental observation[24,25]). Specifically, after water dissociated at the top O atoms, surface −OOH that is formed can then lose its H barrierlessly to form $-OO^-$ (as shown in Figure 4) with bond length 1.28 Å. One evidence showing this

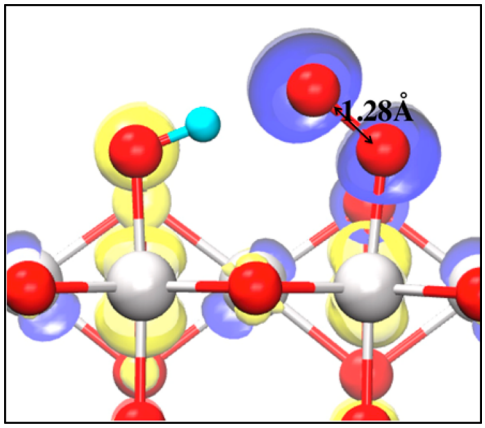

Figure 4. Spin density distribution (spin up−spin down) for surface structure 3 (blue is negative sign; yellow is positive sign). Red balls are O; blue balls are H; silver balls are Ir.

step is barrierless is that with a second layer of explicit H_2O molecules on top of surface we found that the −OOH at structure 2 in Figure 2, will spontaneously lose H to an explicit H_2O molecule then form H_3O^+ and $-OO^-$ at the IrO_2 surface (during geometry optimizations.) Figure 4 shows one unpaired electron distributed at the O−O π^* orbital.

At this high potential (1.53 eV vs NHE) the surface H atoms are removed so that a free OO^- will evolve from the surface to form O_2 molecule while leaving behind an O vacancy. (We found that, without the neighbor H, the free energy to remove O_2 from the surface is decreased by 0.2 eV because the interaction between surface H and O_2 is absent.) Meanwhile, a second aqueous H_2O molecule can bind to the O vacancy site. This leads to an extraordinarily large 0.94 eV H_2O binding energy to the O vacancy site. In a previous study, we also found that the H_2O binding energy at the bare IrO_2 (110) surface is nearly twice that of the bare TiO_2 (110) surface.[20] After H_2O attaches to the vacancy, surface (structure 5 in Figure 2) will be deprotonated to reform the stable O terminated surface.

An alternative path (the red path as shown in Figure 2) is to first protonate the O terminated surface at the top O atom (to form 25% OH terminated surface) then allow an aqueous water molecule to dissociate at the surface. This path is thermodynamically less favorable by 0.13 eV compared with the direct water dissociation path (black path in Figure 2). Interestingly, this second path has a lower reaction barrier by 0.13 eV compared to the direct path, making it kinetically more favorable. (Reactions 1 → 1′and 2′ → 2 are barrierless and kinetically fast processes, similar to what we discussed above.) This result conveys an important message here: the reaction barriers need not be proportional to the reaction energies of the intermediates, a simple concept often assumed to be fundamental in many previous studies of OER mechanism at oxide surfaces, where only the free energies of the intermediates were computed.[3,26,27]

3.2.2. Reaction Path at 1.21 < U < 1.50 eV vs NHE. To complete our mechanistic study, we also investigated the reaction mechanism at the potential less than 1.50 eV (1.36 eV vs NHE), although the experimental potential is larger than 1.5 eV. At this potential, the most stable surface structure is 50% −OH terminated surface at the top O atoms (surface structure 1″ in Figure 5). After the top O attaches an H atom to form

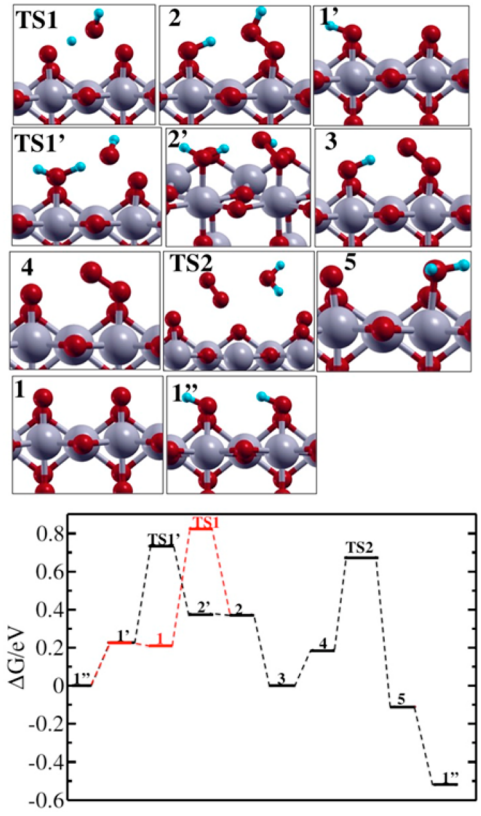

Figure 5. Optimized structure and free energy profile of reaction intermediates and transition states of water dissociation reaction at U = 1.36 eV vs NHE. Red balls are O; blue balls are H; silver balls are Ir.

OH, no unpaired spin is left so that the top O atoms are not reactive anymore. Therefore, in order to form the −OO bond at the surface, we must remove at least one H atom from the top O atoms as shown in Figure 5 (surface structure 1 and 1′).

The black line in Figure 5 shows the reaction path with one surface H removed from 1″ before the H_2O dissociation step; the red line shows both surface H atoms removed from 1″ before H_2O dissociation. For both reaction paths, most intermediates have reaction free energies that are endothermic indicating that at the potential 1.36 eV (<1.50 eV), OER may be slow at the IrO_2 (110) surface. Another important result here is that, as in the case for U > 1.50 eV, the reaction path with slightly more stable intermediates (reaction 1 → 2 compared to 1′ → 2′; for details, see the SI, Table S1), has higher reaction barriers (TS1 compared to TS1′). Again this shows that the reaction steps that are thermodynamically more favorable can be kinetically less favorable.

3.3. Transition States of OER. *3.3.1. Transition States for Water Dissociation.* Next we examine the important transition states in detail (other reaction steps are barrierless). We computed all possible transition state structures of one H_2O molecule dissociated at the IrO_2 (110) O terminated surface as

DOI: 10.1021/jacs.6b07557
J. Am. Chem. Soc. 2017, 139, 149−155

shown in Figure 6. We found although the final state of the "TS1-model2" is 0.2 eV higher than that of the "TS1-model1",

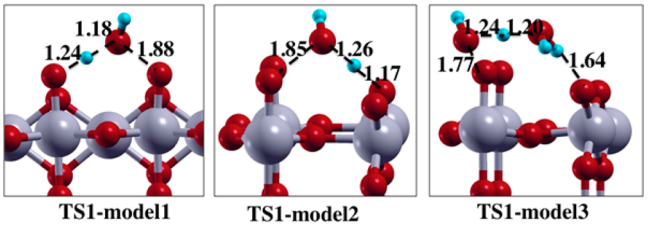

Figure 6. Transition states of water dissociated at the O terminated surface. "TS1-model1" is the transition state of both −OOH and −OH at top O; "TS1-model2" is the transition state of −OOH at the top O and −OH at the bridging O; "TS1-model3" is the transition state of −OOH at the top O and −OH at the bridging O with two explicit water molecules instead of one.

the reaction barriers from the reactants to the transition states are very similar (difference of 10 meV). In order to understand the effect of more explicit water molecules, we added a second water molecule and reexamined the transition state barriers: we found "TS1-model3" has a barrier of 0.61 eV (similar to those of the "TS1-model1" 0.58 eV and the "TS1-model2" 0.59 eV, when all the transition states referenced to the initial state of O terminated surface plus one or two H_2O molecules from the bulk water) at U = 1.53 eV vs NHE. We note that we compared the stability of different water configurations for two H_2O at IrO_2 (110) surface and the initial state for "TS1-model3"gives 0.5−0.7 eV lower energy compared with other configurations (see SI Figure S3 for details). Interestingly, the transition state with two explicit water molecules involves a proton transfer between two water molecules as shown in Figure 6. These results confirm that the reaction barrier of H_2O dissociation is insensitive to the explicit H_2O configuration and number of explicit water molecules in the calculations.

3.3.2. Transition States of O_2 Removal. Removing O_2 from the surface is a nontrivial step involving several complications: (1) it is unclear whether O_2 dissociation from the surface and H_2O binding to the O vacancy is simultaneous or sequential; (2) whether DFT can capture the O_2 spin changes from doublet O_2^- at the surface to triplet O_2 molecule in solution or air; (3) we must consider how to take into account the change of O_2 free energy from the oxide surface to solution or vacuum. We computed the energy barrier of one O_2 substituted by one H_2O molecule using CI-NEB at the PBE+D2 level of theory (structures of the initial state, transition state, and final state are shown in Figure 7). We found an energy barrier of 0.39 eV (if the translational and rotational enthalpy and entropy of O_2 is from the gas phase, computed by Jaguar) and 0.56 eV (if we consider the translational and rotational enthalpy and entropy of O_2 is from 1 M O_2 in liquid H_2O, with 0.17 eV difference from the gas phase, computed by the Henry's law: $\Delta G = -RT \ln K_H$) at U = 1.53 eV vs NHE.

The initial structure has an Ir−O bond length 1.93 Å, while the transition state has an Ir−O bond length 3.16 Å; thus, the explicit water molecule did not participate in the reaction. Instead it has only a van der Waals contact to the surface, at which the energy goes down by 0.94 eV after H_2O comes in and binds to the O vacancy site. (The NEB path is included in the SI, Figure S7.) This is consistent with the hydrophobic character of the O_2 molecule (or low solubility of O_2 in H_2O). Therefore, the H_2O does not interact with the O_2 molecule and

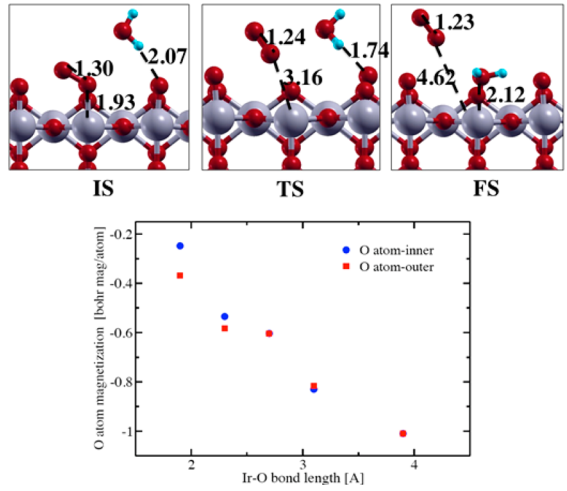

Figure 7. Top: initial, transition state and final structures of the process of one O_2 substitute by a water molecule. Bottom: magnetization of two O atoms (blue dot, O atom attached to the surface; red square, O atom pointing away from the surface) as a function of Ir−O bond length.

instead binds to the surface vacancy site after the O_2 is sufficiently far away (4.62 Å) from the surface.

As discussed above (and shown in Figure 4), O_2 has one unpaired spin when attached to IrO_2 surface. We traced the change of the spins on the two O atoms (computed as Lowdin charges and renormalized by the atomic spin of an isolated O_2 molecule, also computed using the Lowdin charge, in order to remove the error of the absolute values from Lowdin charge) during the process of removing O_2 from the surface as a function of Ir−O atom distance (as shown in the bottom figure of Figure 7). As the Ir−O distance increases from 1.93 to 4 Å, the atomic spin of one O atom increases from ∼0.3 to ∼1.0 au, indicating a *spin doublet to triplet transition for O_2*. Although the PBE+D2 level of theory cannot describe the energy difference of different O_2 electronic states accurately (requiring multi-determinants beyond density function theory to accurately reproduce the difference between the ground triplet state and first excited state), the net spin on the O_2 is described fairly well.

The remaining question is this: What is the rate-determining step (RDS) for the OER reaction at the IrO_2 (110) surface? We found that the water dissociation step has the highest free energy barrier which demonstrates this is the rate-determining step, consistent with the previous results on similar surfaces such as RuO_2 (110) in ref 5. We note that although the PBE-D2 estimate of the barrier for removing O_2 seems fairly high, we also found that O_2 at this level of DFT is overbound, limitation of semi-local functional used in these studies (a more detailed discussion is in the SI Figure S8).

3.4. Microkinetic Model and Comparison With the Experimental Tafel Line. An important advantage of performing calculations at the constant potential condition is that the relationship between the activation energy barrier and the electrochemical potential can be obtained naturally with the surface charges adjusted by the constant potential, with no need to manually introduce charges to the surface as done in ref 18. With the reaction barriers as a function of electrochemical potentials, we can obtain the reaction rates and the currents based on the classical Transition State Theory.

DOI: 10.1021/jacs.6b07557
J. Am. Chem. Soc. 2017, 139, 149−155

In previous studies, only a single reaction barrier has been assumed to be rate determining in predicting reaction rates; however, our study finds two possible reaction paths can coexist at both low (<1.5 eV) and high (>1.5 eV) potentials. Therefore, we considered a more sophisticated microkinetic model to obtain our reaction rates by (more detailed derivation can be found in the SI):

$$R = k_{25}[C_{25}] + k_0[C_0] \quad (2)$$

where R is the reaction rate, $k_{25} = A\exp\left(-\frac{G_{25}(\eta)}{kT}\right)$ based on the transition state theory, A is $\frac{kT}{h} = 6.25 \times 10^{12}$ s^{-1} at the standard condition 298 K and 1 atm, G_{25} is the reaction barrier of the water dissociated at the 25% OH covered surface as a function of overpotential η (defined as the potential relative to 1.23 eV plus NHE), k_{25} is the reaction rate for this particular reaction at one active site, and $[C_{25}]$ is the concentration of active sites at 25% OH terminated surface. The notations for the reaction of water dissociation at the O terminated surfaces (0% OH coverage) k_0, c_0 are analogous. We note that we only considered the reaction rates at 25% OH covered surface and O terminated surfaces because water only dissociates at these two surfaces from our calculations.

We can obtain the concentrations of $[C_{25}]$ and $[C_0]$ from the equilibrium constants between surfaces with different OH coverage concentrations:

$$[M_0] = [C_0] + [C_{25}] + [C_{50}] + [C_{75}] + [C_{100}] \quad (3)$$

where $[M_0]$ is the total concentration of surface active sites, which is a sum of the active sites at different OH coverage. $[M_0]$ can be computed by active sites divided by surface area. The concentrations of $[C_0]$ *and* $[C_{25}]$ can be written by $[M_0]$ based on eq 3 and their surface equilibrium constants:

$$[C_0] = \frac{[M_0]}{1 + K_{025} + K_{050} + K_{075} + K_{0100}} \quad (4)$$

where $K_{025} = C_{25}/C_0$ is the equilibrium constant between 25% OH covered surface and O terminated surface which can be computed by $K_{025} = \exp\left(-\frac{G_{025}(\eta)}{kT}\right)$, analogous to k_{25} we discussed above. We can also express $[C_{25}]$ similarly by combining eq 4 and $K_{025} = C_{25}/C_0$. Afterward we obtain the overall reaction rates by

$$R = \frac{[M_0]k_0 + [M_0]k_{25}K_{025}}{1 + K_{025} + K_{050} + K_{075} + K_{0100}} \quad (5)$$

Finally, we convert reaction rate R to currents in order to compare with experimental electrochemical measurements:

$$\log_{10} j(\eta) = \log_{10}\left(nFN_A^{-1}R(\eta)\right) \quad (6)$$

where n is the charge transfer in OER reaction; F is the Faraday constant, and N_A is the Avogadro constant. Figure 8 shows our calculated relationship between $\log_{10}(j)$ and overpotential η, the Tafel plot.

There are two linear regions before and after ~0.32 V. Below η = 0.26 V, the Tafel slope is 47 mV/dec. This is slightly higher than that reported for IrO_2 nanoparticles (38−45 mV/dec[28]) probably because our calculations assume a very ordered surface.[29] Above 0.38 V, the Tafel slope is 240 mV/dec, because the dominant surface termination evolves from hydroxy to oxo, leading to a different reaction mechanism dominating the reaction, as discussed above.[30]

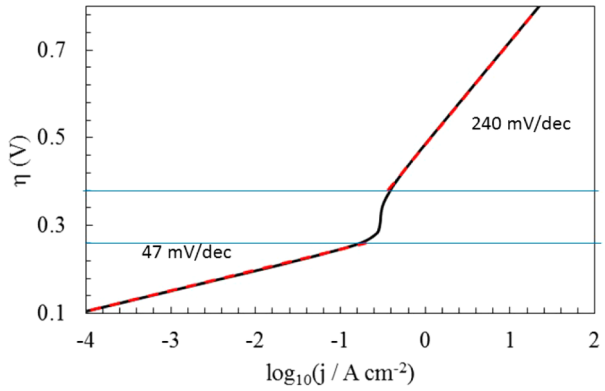

Figure 8. Tafel plot. The black line is the $\log_{10}(j)$ vs overpotential for OER on IrO_2 (110) calculated at the level of PBE-D2 DFT. The red dotted lines show the linear regions in the Tafel plot, which essentially superimpose on the black lines for each region. Below 0.26 V overpotential, the Tafel slope is 47 mV/dec, which can be compared with experimental values of 38−45 mV/dec. In this region our Tafel may be too high because we use a very crystalline surface. Above 0.38 V overpotential, the Tafel slope is 240 mV/dec, indicating the change in the reaction mechanism arising from to the dominant surface termination evolving from hydroxy to oxo.

4. CONCLUSIONS AND OUTLOOK

In this work, we used DFT quantum mechanics in the first investigation of the OER reaction mechanism at the IrO_2 (110) surface including kinetic barriers at constant potential conditions. The computed Tafel slope and overpotentials based on the microkinetic model are in agreement with experimental electrochemical measurements. Our major findings are as follows:

(1) the rate-determining water dissociation step is electrochemically dependent at the constant potential condition (although not at the constant charge condition);
(2) the reaction steps that are thermodynamically favorable are in some cases kinetically less favorable as discussed in subsection 3.3;
(3) O_2 dissociation from the surface goes continuously from a doublet state when bound to the surface to a triplet state at the dissociated state, and H_2O does not bind to the O vacancy site until O_2 is removed from the surface.

The observation that the active sites are the top O atoms with unpaired spins indicates the surface orientation with the maximum number of unsaturated Ir atoms may be the most active. This is because unsaturated Ir atoms on the bare surface will react with H_2O, to form surface OH sites due to the large water binding energy at the IrO_2 surface, which leads to radical character on the surface O after deprotonation at the OER operating potential. This suggests that the less stable (100) IrO_2 surface may be more active than the (110) IrO_2 surface as discussed in ref 30.

The insights from our mechanistic study of IrO_2 (110) surface OER reaction should provide guidance for designing more active catalysts.

DOI: 10.1021/jacs.6b07557
J. Am. Chem. Soc. 2017, 139, 149−155

■ ASSOCIATED CONTENT

Supporting Information

The Supporting Information is available free of charge on the ACS Publications website at DOI: 10.1021/jacs.6b07557.

Atomic coordinates of the structures in Figures 2 and 5 (PDF)

Computational details of DFT calculations performed by Quantum Espresso, JDFTx, Jaguar software; reaction energies and barriers at constant potential and constant charge conditions; surface structure of the O−O coupling intermediate at the IrO_2 (110) surface, other initial geometries for a layer of explicit water at pristine (110) IrO_2 surface, other geometries for the initial states of TS-model 3; work functions of IrO_2 surface during water dissociation reaction; linearity of reaction barrier free energy as a function of the applied potential; CI-NEB path of O_2 removing from IrO_2 surface; details of the microkinetic models; O_2 binding energy to IrO_2 cluster by B3LYP and PBE (PDF)

■ AUTHOR INFORMATION

Corresponding Authors

*yuanping@ucsc.edu

*wag@wag.caltech.edu

ORCID

William A. Goddard III: 0000-0003-0097-5716

Present Address

§Y.P.: The Department of Chemistry and Biochemistry, University of California, Santa Cruz.

Notes

The authors declare no competing financial interest.

■ ACKNOWLEDGMENTS

We thank Dr. Ravishankar Sundararaman, Dr. Hai Xiao, Dr. Tao Cheng, and Dr. Yan Choi Lam for useful discussions. This paper is based on work performed in Joint Center for artificial photosynthesis—a DOE innovation hub, supported through the Office of Science of the U.S. Department of Energy under Award Number DE-SC0004993. This research used resources of the National Energy Research Scientific Computing Center, a DOE Office of Science User Facility supported by the Office of Science of the U.S. Department of Energy under Contract No. DE-AC02-05CH11231.

■ REFERENCES

(1) Walter, M. G.; Warren, E. L.; McKone, J. R.; Boettcher, S. W.; Mi, Q. X.; Santori, E. A.; Lewis, N. S. *Chem. Rev.* **2010**, *110*, 6446.

(2) Ma, T. Y.; Cao, J. L.; Jaroniec, M.; Qiao, S. Z. *Angew. Chem., Int. Ed.* **2016**, *55*, 1138.

(3) Jiao, Y.; Zheng, Y.; Jaroniec, M.; Qiao, S. Z. *Chem. Soc. Rev.* **2015**, *44*, 2060.

(4) Kumar, B.; Llorente, M.; Froehlich, J.; Dang, T.; Sathrum, A.; Kubiak, C. P. *Annu. Rev. Phys. Chem.* **2012**, *63*, 541.

(5) Rossmeisl, J.; Qu, Z. W.; Zhu, H.; Kroes, G. J.; Norskov, J. K. *J. Electroanal. Chem.* **2007**, *607*, 83.

(6) Rossmeisl, J.; Logadottir, A.; Norskov, J. K. *Chem. Phys.* **2005**, *319*, 178.

(7) Man, I. C.; Su, H. Y.; Calle-Vallejo, F.; Hansen, H. A.; Martinez, J. I.; Inoglu, N. G.; Kitchin, J.; Jaramillo, T. F.; Norskov, J. K.; Rossmeisl, J. *ChemCatChem* **2011**, *3*, 1159.

(8) Sundararaman, R.; Goddard, W. A., III; Arias, T. A. Under preparation, 2016.

(9) Xiao, H.; Cheng, T.; Goddard, W. A.; Sundararaman, R. *J. Am. Chem. Soc.* **2016**, *138*, 483.

(10) Spurgeon, J. M.; Velazquez, J. M.; McDowell, M. T. *Phys. Chem. Chem. Phys.* **2014**, *16*, 3623.

(11) Ping, Y.; Goddard, W. A.; Galli, G. A. *J. Am. Chem. Soc.* **2015**, *137*, 5264.

(12) Garrity, K. F.; Bennett, J. W.; Rabe, K. M.; Vanderbilt, D. *Comput. Mater. Sci.* **2014**, *81*, 446.

(13) Giannozzi, P.; et al. *J. Phys.: Condens. Matter* **2009**, *21*, 295502. Giannozzi, P.; Baroni, S.; Bonini, N.; Calandra, M.; Car, R.; Cavazzoni, C.; Ceresoli, D.; Chiarotti, G. L.; Cococcioni, M.; Dabo, I.; Dal Corso, A.; de Gironcoli, S.; Fabris, S.; Fratesi, G.; Gebauer, R.; Gerstmann, U.; Gougoussis, C.; Kokalj, A.; Lazzeri, M.; Martin-Samos, L.; Marzari, N.; Mauri, F.; Mazzarello, R.; Paolini, S.; Pasquarello, A.; Paulatto, L.; Sbraccia, C.; Scandolo, S.; Sclauzero, G.; Seitsonen, A. P.; Smogunov, A.; Umari, P.; Wentzcovitch, R. M. *J. Phys.: Condens. Matter* **2009**, *21*, 395502.

(14) Grimme, S. *J. Comput. Chem.* **2006**, *27*, 1787.

(15) Henkelman, G.; Uberuaga, B. P.; Jonsson, H. *J. Chem. Phys.* **2000**, *113*, 9901.

(16) Baroni, S.; de Gironcoli, S.; Dal Corso, A.; Giannozzi, P. *Rev. Mod. Phys.* **2001**, *73*, 515.

(17) Bochevarov, A. D.; Harder, E.; Hughes, T. F.; Greenwood, J. R.; Braden, D. A.; Philipp, D. M.; Rinaldo, D.; Halls, M. D.; Zhang, J.; Friesner, R. A. *Int. J. Quantum Chem.* **2013**, *113*, 2110.

(18) Fang, Y. H.; Liu, Z. P. *J. Am. Chem. Soc.* **2010**, *132*, 18214.

(19) Sundararaman, R.; Goddard, W. A. *J. Chem. Phys.* **2015**, *142*, 064107.

(20) Ping, Y.; Sundararaman, R.; Goddard, W. A., III *Phys. Chem. Chem. Phys.* **2015**, *17*, 30499.

(21) Letchworth-Weaver, K.; Arias, T. A. *Phys. Rev. B: Condens. Matter Mater. Phys.* **2012**, *86*, 075140.

(22) Gunceler, D.; Letchworth-Weaver, K.; Sundararaman, R.; Schwarz, K. A.; Arias, T. A. *Modell. Simul. Mater. Sci. Eng.* **2013**, *21*, 074005.

(23) Norskov, J. K.; Rossmeisl, J.; Logadottir, A.; Lindqvist, L.; Kitchin, J. R.; Bligaard, T.; Jonsson, H. *J. Phys. Chem. B* **2004**, *108*, 17886−17892.

(24) McCrory, C. C. L.; Jung, S. H.; Peters, J. C.; Jaramillo, T. F. *J. Am. Chem. Soc.* **2013**, *135*, 16977.

(25) McCrory, C. C. L.; Jung, S.; Ferrer, I. M.; Chatman, S. M.; Peters, J. C.; Jaramillo, T. F. *J. Am. Chem. Soc.* **2015**, *137*, 4347.

(26) Ling, C.; Zhou, L. Q.; Jia, H. F. *RSC Adv.* **2014**, *4*, 24692.

(27) Zhang, P. X.; Dong, Y.; Kou, Y. L.; Yang, Z. Y.; Li, Y. P.; Sun, X. M. *Catal. Lett.* **2015**, *145*, 1169.

(28) Abbott, D. F.; Lebedev, D.; Waltar, K.; Povia, M.; Nachtegaal, M.; Fabbri, E.; Coperet, C.; Schmidt, T. J. *Chem. Mater.* **2016**, *28*, 6591.

(29) Smith, R. D. L.; Sporinova, B.; Fagan, R. D.; Trudel, S.; Berlinguette, C. P. *Chem. Mater.* **2014**, *26*, 1654.

(30) Stoerzinger, K. A.; Qiao, L.; Biegalski, M. D.; Shao-Horn, Y. *J. Phys. Chem. Lett.* **2014**, *5*, 1636.

DOI: 10.1021/jacs.6b07557
J. Am. Chem. Soc. 2017, 139, 149−155